Nanocomposites

DOI: 10.1002/anie.201400490

Doubling the Capacity of Lithium Manganese Oxide Spinel by a Flexible Skinny Graphitic Layer**

Hyun Kuk Noh, Han-Saem Park, Hu Young Jeong, Sang Uck Lee, and Hyun-Kon Song**

Abstract: *By coating nanoparticular lithium manganese oxide (LMO) spinel with a few layers of graphitic basal planes, the capacity of the material reached up to 220 mA h g^{-1} at a cutoff voltage of 2.5 V. The graphitic layers 1) provided a facile electron-transfer highway without hindering ion access and, more interestingly, 2) stabilized the structural distortion at the 3 V region reaction. The gain was won by a simple method in which microsized LMO was ball-milled in the presence of graphite with high energy. Vibratory ball milling pulverized the LMO into the nanoscale, exfoliated graphite of less than 10 layers and combined them together with an extremely intimate contact. Ab initio calculations show that the intrinsically very low electrical conductivity of the tetragonal phase of the LMO is responsible for the poor electrochemical performance in the 3 V region and could be overcome by the graphitic skin strategy proposed.*

It cannot be overemphasized that improving transport of charge carriers is important to attain superior performances in electrochemical cells such as batteries, fuel cells, and solar cells. Electrons should reach faradaic reaction points in a facile way through conductive percolation routes, overcoming charge-transfer resistance involved. Simultaneously, ionic transport also should be guaranteed into the reaction points. $LiFePO_4$ olivine as a cathode material of lithium-ion batteries (LIBs) is one of the representative examples that amorphous carbon coating drives successful commercialization by enhancing electric conductance.[1] However, the amorphous carbon coating that is obtained by pyrolysis of carbon precursors under inert atmosphere is not applicable to widely used oxide electrode materials such as lithium manganese oxide spinel (LMO) and layered lithium nickel–manganese–cobalt oxide (LNMC). The oxides suffer from severe negative effects during the thermal treatment, experiencing change in the oxidation state of the transition metal and the crystal structure.[2] Therefore, a more versatile as well as non-degenerating strategy is required for coating electroactive materials with conductive materials.

Herein, we report on a strategy to tether a-few-layer flexible graphitic skin conformally onto the surface of LMO. Microsized bare LMO was ball-milled with graphite in a vibratory ball mill (known to be more energetic than planetary ones) under inert atmosphere (Figure 1), turning into nanosized LMO with the graphitic skin (LMO@Gn).

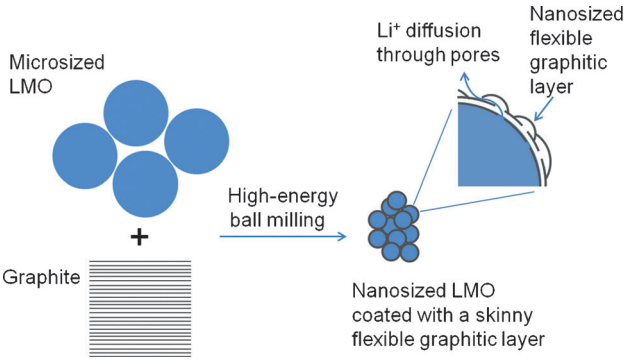

Figure 1. High-energy ball-milling process to tether a-few-layer nanosized flexible graphitic skin onto the surface of nanoparticular LMO.

Several processes proceeded simultaneously: nanosizing of LMO, pulverization of graphite into exfoliated graphene sheets (Gn), and attachment of Gn onto the activated surface of LMO. A-few-layer Gn have received great attention because of their excellent structural and electronic properties.[3] Recently, it was reported that Gn can be prepared by planetary ball milling in the presence of exfoliating agents (e.g., CO_2, NH_3, Cl_2, and SO_3).[4] Without the exfoliating agents, however, we succeeded in producing the few-layer Gn because of the high-energy impact of the vibratory ball mill.

Before compositing Gn with nanoparticular LMO, feasibility on formation of Gn by high-energy ball milling was confirmed (Figure 2 and Figure S1 in the Supporting Information). By 1 h of ball milling, flat Gn consisting of 4 to 12 graphene layers with larger dimension were mainly observed (Figure 2a and c and Figure S1a and b), succeeding to morphology of original graphite (Figure S1e). By longer ball milling for 6 h, however, a more winding and curved morphology of smaller dimensions developed, although flat

[*] Dr. H. K. Noh, H.-S. Park, Prof. H.-K. Song
School of Energy and Chemical Engineering, UNIST
Ulsan, 689-798 (Korea)
E-mail: hknoh21@gmail.com
philiphobi@hotmail.com
Prof. H. Y. Jeong
UNIST Central Research Facilities (UCRF)
UNIST, Ulsan 689-798 (Korea)
Prof. S. U. Lee
Department of Chemistry, University of Ulsan
Ulsan 680-749 (Korea)

[**] This work was supported by MOTIE (Green: grant number 10042948 (KEIT)), MSIP (Mid: grant number 2013R1A2A2A04015706 (NRF), CRC: grant number 2013K000210) and MOE (BK21Plus: grant number 10Z20130011057), Korea. The authors thank for support from the Center for Computational Materials Science (Institute for Materials Research, Tohoku University; SR11000 supercomputing facilities).

Supporting information for this article is available on the WWW under http://dx.doi.org/10.1002/anie.201400490.

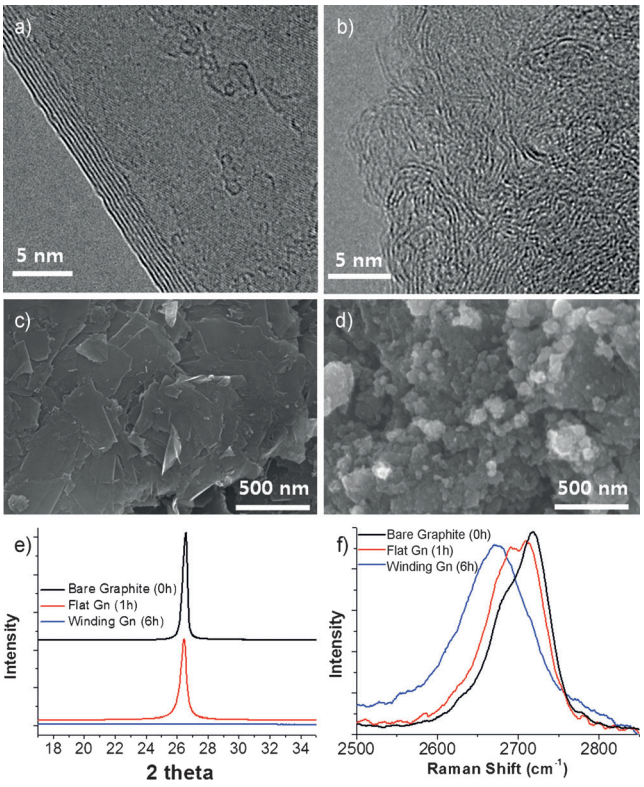

Figure 2. Graphitic nanosheets (Gn) prepared by high-energy ball-milling graphite. a–d) Electron-microscopic images of 1 h-milled (a and c) and 6 h-milled Gn (b and d). Transmission (TEM, a and b) and scanning electron microscope (SEM, c and d) were employed. Flat Gn of larger size were mainly obtained by 1 h of milling whereas smaller winding Gn dominantly formed by 6 h of milling. e) XRD patterns. f) 2D bands in Raman spectra. Deconvolution of the bands is presented in Figure S1.

Gn of 3 to 8 layers was occasionally observed (Figure 2b and d, Figure S1c and d). The winding morphology implies the mechanically flexible nature of the Gn guaranteeing intimate contact with the rough surface of the substrate. The intensity of the (002) graphitic peak at 2θ of about 26.4° in the X-ray diffractogram decreased substantially with increasing ball-milling time, indicating that the number of graphene layers is reduced (Figure 2e). No peak was observed after 6 h of ball milling, because the long-range-ordered structure was lost. Accordingly, the D/G ratio of the Raman spectra increased substantially with increased ball-milling time (Figure S1f). In addition, the shape of the 2D Raman bands of the ball-milled graphites was significantly different from that of bare graphite (Figure 2f and Figure S1g to i). Bare graphite showed an asymmetric 2D band consisting of two different Lorentzian peaks whereas the bands of the ball-milled graphite samples were more symmetric. The shape of the 2D band of flat Gn (1 h-milled) corresponds to that of 4-to-6-layer Gn,[5] deconvoluted to one major Lorentzian peak and another minor one. The 2D band of winding Gn (6 h-milled) was fitted by a single Lorentzian peak and showed a red shift to the peak position of single-layer graphene (2675 cm^{-1}) indicating (002) interlayer expansion or complete exfoliation by extensive ball milling.[5–6] The specific surface area was determined at 19 $m^2 g^{-1}$ (bare graphite), 100 $m^2 g^{-1}$ (flat Gn), and 270 $m^2 g^{-1}$ (winding Gn), supporting exfoliation of graphite into a few layer Gn.

Subsequently, a mixture of graphite and bare LMO (Al-doped or undoped) was ball-milled for 1 or 6 h to coat the bare LMO with Gn. For comparison, only the bare LMO was also ball-milled in absence of graphite for 1 or 4 h. Only a limited number of articles reported on graphitic layer coating onto electroactive particles by ball milling.[7] However, it is unclear that the intimate contact between the graphitic layers and active materials resulting in an enhanced charge transfer was achieved by such low-energy ball milling used in the previous works. The high-energy ball milling we adopted in this work realized more conformal and skinny graphitic layer coating onto nanoparticular LMO (Figure 3a to c and Figure S2a and b). Production of thin or winding Gn and their adaptability to surface geometry of substrate are key advantages of high-energy (vibratory) ball milling compared with its low-energy (planetary) counterpart (Figure S3).

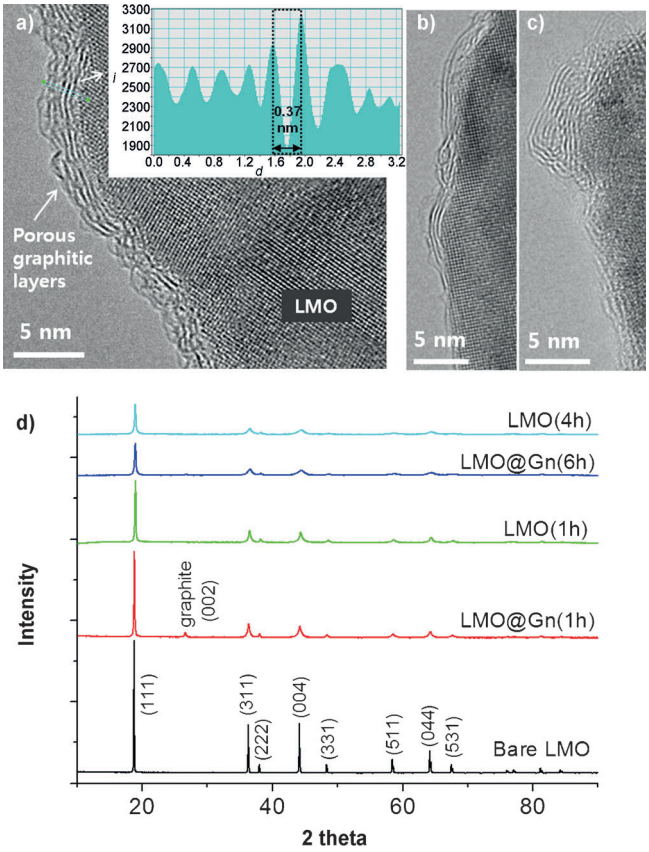

Figure 3. LMO@Gn prepared by high-energy ball milling microsized LMO with graphite. a–c) TEM images of LMO@Gn. The graphitic-layer-skinned LMOs were obtained by ball milling for 1 h (a and b) and 6 h (c). Al-doped LMO was used for (b) and (c) while undoped LMO was used for (a). a) A higher value of the d_{002} interlayer distance (0.37 nm; see inset; d = distance in nanometer and i = intensity) from the ordinary one (0.335 nm) is due to interlayer expansion by ball milling.[5–6] d) XRD patterns of Al-doped LMO ball milled in the absence or presence of graphite. Ball-milling times were indicated in parentheses after LMO. Bare LMO is the microsized Al-doped LMO before ball milling.

Collision during the high-energy ball mill process further fits the flexible Gn on active materials. However, thicker and mechanically rigid Gn produced by low-energy ball milling leads to poor contact to the rough surface with insufficient adaptability onto the surface geometry.[6,7] In addition, porous structure of layered Gn of small dimension formed by the high-energy ball milling facilitates Li ion transport at the electrode–electrolyte interface. If non-porous graphene layers of larger size were employed on a flat surface (Figure S3c), the Li-ion diffusion would be severely inhibited. It was found that all LMO@Gn(6 h) nanoparticles were covered with graphitic layers on their surface, while the coverage of graphitic layers on LMO@Gn(1 h) nanoparticles was about 25% indicating that the coverage significantly depends on the ball-milling time.

XRD analysis revealed that nanodomain and microstrain (ε_0) were developed with peaks broadening after ball milling, while lattice parameters of LMO (in the bare Al-doped LMO and its ball-milled and Gn-coated versions) were not significantly changed (Figure 3d, Figure S2c, and Table S1).[8] No structural changes were also true with the same series of undoped LMO. In terms of particle size, lattice parameter, and microstrain, 4 h-milled LMO was equivalent to 6 h-milled LMO@Gn whereas the milling time of 1 h led to almost identical physical parameters for both ball-milled LMO and LMO@Gn. SEM analysis showed that the bare LMO particles were pulverized from 2–3 μm to 100–150 nm or 50–100 nm by ball milling for 1 or 6 h (4 h for LMO), respectively (Figure S2d to h).

The graphitic skin showed multiple functions not only as a conductive but also as a chemical-protective layer. Acidic delithiation of LMO@Gn (6 h-milled) and LMO (4 h-milled) were performed.[9] The particle size of the two different samples was confined between 50 and 100 nm to make the size effect negligible. Lattice parameters of LMO@Gn(6 h) and LMO(4 h) after the treatment were determined to be 8.100 and 8.073 Å respectively (compare to 8.203 Å for LMO without acid treatment), indicating that graphene-skinned LMO is more endurable against acidic attack (Figure S2i). Therefore, the well-known disproportionation reaction ($2\,Mn^{3+} \rightarrow Mn^{2+}(\text{soluble}) + Mn^{4+}$) catalyzed by acid in electrolyte can be suppressed by the graphitic coating, which leads to prolonged cycle retention.

LMO is one of the most widely used cathode materials of LIBs. Li^+ insertion into the spinel framework ($Li_y[Mn_2]O_4$ with $0 < y < 1$ in the cubic phase) in the 4 V region is responsible for the main faradaic process delivering more than 100 mA h g^{-1} (4 V region capacity, Q_{4V}). The second reaction with $1 < y < 2$ is evolved around 2.9 V with additional capacity at >100 mA h g^{-1} (3 V region capacity, Q_{3V}).[10] The tetragonal phase is developed in the two-phase 3 V region reaction, increasing its crystallographic axial ratio (c/a) from 1.0 to 1.16. Accordingly, the capacity fades seriously with a fracture of the LMO particles, which is one of the reasons why the 3 V-level reaction cannot be used practically.

Electrochemical properties of LMO@Gn and LMO were studied (Figure 4). Al-doped LMOs were mainly investigated for electrochemical studies because undoped LMOs showed a relatively poor performance in the 4 V region: 105 mA h g^{-1} for Al-doped LMO (bare) versus 80 mA h g^{-1} for undoped LMO (bare) with a poorer cycle capability than Al-doped LMO (bare) at 0.5 C. In the 3 V region, nanosizing and the graphitic skin not only increased the capacity but also enhanced its retention with cycles (Figure 4a and b). Ball milling of only LMO increased discharge capacity from 18 mA h g^{-1} (bare LMO) to about 70 mA h g^{-1} (4 h-milled LMO without graphite) with slow capacity fading after the 20th cycle. Kang et al. pointed out that nanograins and microstrain developed by ball milling are the main reasons responsible for the improvement of cycle capability in the 3 V region.[10b] Smaller particles or grains within particles experience less anisotropic deformation caused by the transition from cubic to tetragonal phase. However, improvement obtained with LMO@Gn surpassed the enhancement induced only by the nanosizing. The capacity of LMO@Gn increased continuously up to the 70th cycle, reaching 103 mA h g^{-1}. The enhanced performances of LMO@Gn originate from highly conductive network represented by the interparticular graphitic skin located between different LMO particles (Figure 4c). In nanosized electrode materials like our ball-milled LMO, contribution of the interparticular electron transport (or electronic contact between particles) is amplified compared to intraparticular one. Enhanced physical integrity of particles achieved by wrapping LMO particles with the graphitic layer is also one of the reasons for the improved capacity retention of LMO@Gn. It should be noted that ball-milled nanosized

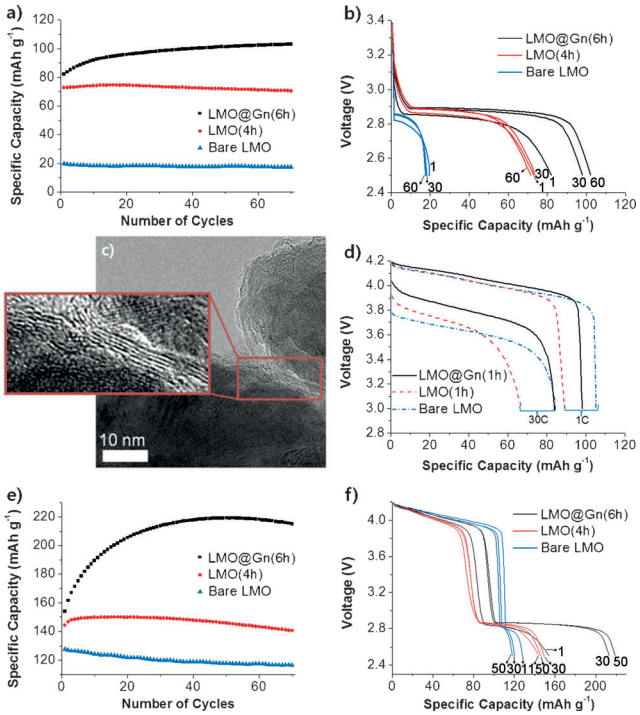

Figure 4. Electrochemical performances of LMO@Gn. a) Discharge capacity recorded with cycles in the 3 V region at 0.5 C. b) Voltage profiles at the 1st, 30th, and 60th cycle of (a). c) TEM image of 6 h-milled LMO@Gn. Two LMO@Gn particles were connected through a graphitic skin. d) Voltage profiles at 1 and 30 C in a 4 V region. e) Discharge capacity recorded with cycles in a 3 + 4 V region at 0.5 C. f) Voltage profiles of the 1st, 30th, and 50th cycle of (e).

LMOs (LMO(4 h) and LMO@Gn(6 h)) exhibited higher working voltage than bare microsized LMO (Figure 4b). Initial IR drop would become smaller with smaller particle size of LMO if their resistances are connected to each other in parallel (Figure S4). The 1 h-milled LMO@Gn and its non-Gn control (LMO(1 h)) showed cycle capability inferior to LMO@Gn(4 h) and LMO(6 h), respectively (Figure S5a). This might be attributed to less coverage ($\approx 25\,\%$) of the Gn layer onto LMO by ball milling for the short time.

The 4 V region reaction also improved with LMO@Gn-(1 h) (Figure 4d) in terms of working potential and rate capability. Like the 3 V region, ball-milled LMO (LMO@Gn-(1 h) and LMO(1 h)) demonstrated significantly higher working voltage than bare LMO in the 4 V region, suggesting again that the higher voltage fairly comes from the smaller size of LMO. LMO@Gn(1 h) exhibited substantially higher working voltage than LMO(1 h) thanks to the graphitic skin: 3.80 V for LMO@Gn(1 h), 3.67 V for LMO(1 h), and 3.63 V for bare LMO at $40\,mA\,h\,g^{-1}$ with 30 C discharge. Enhancement of rate-dependent retention of capacity (or rate capability) was also significant with the graphitic coating (Figure S6): 71 % for LMO@Gn(1 h) versus 66 % for bare LMO and 62 % for LMO(1 h) at 60 C rate. The 6 h-milled LMO@Gn and its non-Gn control (LMO(4 h)) did not reach the same level of enhancement of LMO@Gn(1 h) and LMO(1 h) (Figure S5b). This could be due to the formation of agglomerate by longer-time ball milling (discussed below).

By combining Q_{4V} with Q_{3V}, LMO@Gn(6 h) delivered up to $220\,mA\,h\,g^{-1}$ with 2.5 V cutoff voltage (Figure 4e and f). The value is two times as large as the capacity practically obtained with LMO at 3.0 V cutoff volatge. Because the cutoff voltage can be practically lowered up to at least 2.7 V, the $200\,mA\,h\,g^{-1}$ level cathode material can be realized by tethering nanosized LMO with skinny graphitic layer. To fully use the $220\,mA\,h\,g^{-1}$, an extra lithium source is required for the 3 V region reaction. Stabilized lithium metal powders (SLMP) with anode materials or overlithiated cathode precursors such as $xLi_2MnO_3{\cdot}(1-x)LiMO_2$ (M = Mn, Ni, Co) or Li_5FeO_4 with LMO can provide additional lithium ions for the 3 V region reaction of LMO.[11]

The increases of capacity during initial cycles (Figure 4e) have been often observed when ball-milled electroactive materials are employed.[10b,12] Two processes are competitive and complementary during ball milling: fracture and welding.[13] The nanosized particles (ball-milled LMO or LMO@Gn here) generated by the fracture process are closely packed to form dense agglomerates. For the electrolyte it is difficult to penetrate into the interior active mass of the agglomerates. As charge/discharge cycles proceed, the densified integrity between primary particles becomes looser and disintegrated because of the volume change caused by the transition between the cubic and the tetragonal phases. With repeated charging and discharging, ionic pathways are more developed whereas electric network wiring active mass to electric pathways provided by carbon black is less encouraged. The Gn layer of LMO@Gn(6 h) provides more robust electric wiring during the disintegration so that much more significant capacity increase is observed in the initial period of cycles compared with LMO(4 h). After the 60th cycle, however, even LMO@Gn(6 h) showed a slight but continuous decrease of the capacity probably because the electric network through Gn and carbon black was deteriorated. By introducing a larger amount of Gn coating or conducting agent, the problem was significantly corrected (Figure S7).

The effect of graphitic coating was more pronounced in the 3 V region than in the 4 V region: $\Delta Q_{4V} = 15\,mA\,h\,g^{-1}$ versus $\Delta Q_{3V} = 55\,mA\,h\,g^{-1}$ between LMO@Gn(6 h) and LMO(4 h) (Figure 4f). We expect this might come from an intrinsic difference in the electric conductivity of the cubic (SPC) and tetragonal (SPT) structures. The intrinsic electrical natures of SPC and SPT materials were computationally elucidated by using the Boltzman transport equation with the rigid band approach (Table 1 and Figure S8).[14] SPC has relatively large electrical conductivity around the Fermi level ($10–10^3\,S\,cm^{-1}$) where the frontier orbitals work as electron transport channels. However, SPT shows a much lower electrical conductivity ($10^{-4}–10^{-3}\,S\,cm^{-1}$), four to seven orders of magnitude smaller than SPC. As the SPT phase is located on the shell region during the discharging process in the 3 V two-phase reaction, it becomes obstacle of electrical conduction in a LMO particle resulting in a fall of electrochemical performance in the 3 V region. Therefore, it is clear that the graphitic skin on nanosized LMO dramatically enhances the electrochemical performance of the 3 V region by improving the electron transport.

Table 1: Intrinsic electrical conductivity of SPC (cubic) and SPT (tetragonal) spinels calculated by ab initio calculation. Al- and Li-doped spinel corresponds to $Li_x(Li_{0.125}Al_{0.125}Mn_{1.75})O_4$ where $x = 1$ for SPC or 2 for SPT.

	Electric conductivity [$S\,cm^{-1}$]
SPC (undoped)	$10^2–10^3$
SPC (Al and Li doped)	$10–10^2$
SPT (undoped or Al and Li doped)	$10^{-4}–10^{-3}$

In this work, we successfully demonstrated the doubling of the capacity of LMO by proposing a strategy to operate efficiently and stably an additional reaction in the 3 V region. Synergistic effects of nanosizing LMO and the graphitic skin in LMO@Gn were responsible for the improved electrochemical performances. A high-energy ball-milling process played an important role of compositing LMO and Gn with a good contact, producing flexibly winding skinny Gn that can be conformally coated on the highly curved surface of the substrate. The Gn-skin strategy based on high-energy ball milling can be applied to other electrode materials for lithium ion batteries (e.g., LNMC and silicon) as well as fuel cells and solar cells, enhancing their performances.

Experimental Section

Sample preparation: Graphite (Timcal KS6), undoped LMO (Aldrich) and Al-doped LMO (Nikki) were used as received. Atomic composition of Al-doped LMO is $Li(Li_{0.1}Al_{0.1}Mn_{1.8})O_4$, which is measured by inductively coupled plasma atomic emission spectroscopy (ICP-AES). LMO indicates the Al-doped LMO (Nikki) unless mentioned otherwise. A mixture of LMO and graphite (80:7

wt/wt) was ball-milled in a stainless vial with balls by using a high-energy vibratory ball miller (SPEX 8000D). The mass ratio of ball to powder was about 1:2. The vial was filled with argon to minimize the oxidation of materials. For acidic delithiation of LMO, 0.1088 g of LMO@Gn(6 h) and 0.1 g of LMO(4 h) were dispersed in 10 mL of 0.2 M HCl solution and reacted for 16 h with stirring at room temperature. After the reaction, the solid phase was collected by centrifuge and analyzed by XRD after drying.

Electrochemical characterization: 2032 coin half cells were employed. Active materials, graphite (when LMO@Gn was not used as the active material), carbon black (Timcal Super P), and polyvinylidene fluoride (PVdF; Kureha KF1100) were mixed with N-methyl-2-pyrrolidone as solvent. The resultant mass composition of the cathode composites was fixed at 80:7:7:6 for LMO/graphite/carbon black/PVdF. A 0.5 C rate corresponds to 60 $mA\,g^{-1}$, 55 $mA\,g^{-1}$, and 115 $mA\,g^{-1}$ for the 3 V, 4 V, and 3 + 4 V regions, respectively.

Computational methods: Ab initio calculations were carried out using the Vienna ab initio simulation package (VASP) at the projector augmented wave (PAW) method with the generalized gradient approximation including the Hubbard U correlation (GGA + U). The Boltzmann transport equation and the rigid band approach have been used to calculate the transport properties. The details of the calculation procedure have been reviewed in the literature.[14]

Received: January 16, 2014
Published online: April 6, 2014

Keywords: ab initio calculations · graphitic layers · lithium-ion batteries · lithium manganese oxide · spinel

[1] a) H.-K. Song, K. T. Lee, M. G. Kim, L. F. Nazar, J. Cho, *Adv. Funct. Mater.* **2010**, *20*, 3818 – 3834; b) N. Ravet, S. Besner, M. Simoneau, A. Vallee, M. Armand, J.-f. Magnan, EP1049182A2, **2000**.

[2] a) G. G. Amatucci, N. Pereira, T. Zheng, J. M. Tarascon, *J. Electrochem. Soc.* **2001**, *148*, A171; b) Y. Gao, J. R. Dahn, *Solid State Ionics* **1996**, *84*, 33 – 40.

[3] a) K. S. Novoselov, A. K. Geim, S. V. Morozov, D. Jiang, Y. Zhang, S. V. Dubonos, I. V. Grigorieva, A. A. Firsov, *Science* **2004**, *306*, 666 – 669; b) S. Stankovich, D. A. Dikin, R. D. Piner, K. A. Kohlhaas, A. Kleinhammes, Y. Jia, Y. Wu, S. T. Nguyen, R. S. Ruoff, *Carbon* **2007**, *45*, 1558 – 1565; c) K. S. Kim, Y. Zhao, H. Jang, S. Y. Lee, J. M. Kim, K. S. Kim, J. H. Ahn, P. Kim, J. Y. Choi, B. H. Hong, *Nature* **2009**, *457*, 706 – 710.

[4] a) T. Lin, J. Chen, H. Bi, D. Wan, F. Huang, X. Xie, M. Jiang, *J. Mater. Chem. A* **2013**, *1*, 500; b) I. Y. Jeon, Y. R. Shin, G. J. Sohn, H. J. Choi, S. Y. Bae, J. Mahmood, S. M. Jung, J. M. Seo, M. J. Kim, D. W. Chang, L. M. Dai, J. B. Baek, *Proc. Natl. Acad. Sci. USA* **2012**, *109*, 5588 – 5593.

[5] a) A. C. Ferrari, *Solid State Commun.* **2007**, *143*, 47 – 57; b) J. H. Lee, D. W. Shin, V. G. Makotchenko, A. S. Nazarov, V. E. Fedorov, Y. H. Kim, J.-Y. Choi, J. M. Kim, J.-B. Yoo, *Adv. Mater.* **2009**, *21*, 4383 – 4387; c) D. Yoon, H. Moon, H. Cheong, J. S. Choi, J. A. Choi, B. H. Park, *J. Korean Phys. Soc.* **2009**, *55*, 1299 – 1303.

[6] a) N. J. Welham, V. Berbenni, P. G. Chapman, *J. Alloys Compd.* **2003**, *349*, 255 – 263; b) F. Salver-Disma, J. M. Tarascon, C. Clinard, J. N. Rouzaud, *Carbon* **1999**, *37*, 1941 – 1959; c) F. Salver-Disma, A. Du Pasquier, J. M. Tarascon, J. C. Lassegues, J. N. Rouzaud, *J. Power Sources* **1999**, *81*, 291 – 295.

[7] a) X. Chen, X. Li, F. Ding, W. Xu, J. Xiao, Y. Cao, P. Meduri, J. Liu, G. L. Graff, J. G. Zhang, *Nano Lett.* **2012**, *12*, 4124 – 4130; b) Z. X. Chen, M. Zhou, Y. L. Cao, X. P. Ai, H. X. Yang, J. Liu, *Adv. Energy Mater.* **2012**, *2*, 95 – 102; c) Z. Chen, Y. Cao, J. Qian, X. Ai, H. Yang, *J. Mater. Chem.* **2010**, *20*, 7266.

[8] G. K. Williamson, W. H. Hall, *Acta Metall.* **1953**, *1*, 22 – 31.

[9] A. Romero-Núñez, A. Ibarra-Palos, *ECS Trans.* **2011**, *36*, 45 – 51.

[10] a) J. Kim, A. Manthiram, *Electrochem. Solid-State Lett.* **1999**, *2*, 55 – 57; b) S. H. Kang, J. B. Goodenough, L. K. Rabenberg, *Chem. Mater.* **2001**, *13*, 1758 – 1764; c) S. H. Kang, J. B. Goodenough, *J. Electrochem. Soc.* **2000**, *147*, 3621 – 3627.

[11] a) C. R. Jarvis, M. J. Lain, M. V. Yakovleva, Y. Gao, *J. Power Sources* **2006**, *162*, 800 – 802; b) M. M. Thackeray, C. S. Johnson, J. T. Vaughey, N. Li, S. A. Hackney, *J. Mater. Chem.* **2005**, *15*, 2257 – 2267; c) C. S. Johnson, S. H. Kang, J. T. Vaughey, S. V. Pol, M. Balasubramanian, M. M. Thackeray, *Chem. Mater.* **2010**, *22*, 1263 – 1270.

[12] a) M. Gauthier, D. Mazouzi, D. Reyter, B. Lestriez, P. Moreau, D. Guyomard, L. Roue, *Energy Environ. Sci.* **2013**, *6*, 2145 – 2155; b) C. H. Doh, A. Veluchamy, D. J. Lee, J. H. Lee, B. S. Jin, S. I. Moon, C. W. Park, D. W. Kim, *Bull. Korean Chem. Soc.* **2010**, *31*, 1257 – 1261.

[13] a) D. L. Zhang, *Prog. Mater. Sci.* **2004**, *49*, 537 – 560; b) N. Eom, M. H. Bhuiyan, T. S. Kim, S. J. Hong, *Mater. Trans.* **2011**, *52*, 1674 – 1678.

[14] G. K. H. Madsen, D. J. Singh, *Comput. Phys. Commun.* **2006**, *175*, 67 – 71.

